Molecular Interactions Underlying Dissolution Trends in Cannabidiol-Polymer Amorphous Solid Dispersions

Baris E. Ugur, Nicholas J. Caggiano, Stephanie Monson, Alexander G. Bechtold, Yejoon Seo, Robert K. Prud'homme, Rodney D. Priestley, and Michael A. Webb*

Department of Chemical and Biological Engineering, Princeton University, Princeton, NJ, 08544, USA

E-mail: mawebb@princeton.edu

Abstract

Cannabidiol (CBD) is viewed as promising therapeutic agent against a variety of health ailments; however, its efficacy is limited by poor aqueous solubility. Amorphous solid dispersions (ASDs) can enhance the solubility of therapeutics by distributing it throughout a polymer matrix. In consideration of ASD formulations with CBD, we investigate the interactions of CBD with various polymers: polyvinylpyrrolidone (PVP), polyvinylpyrrolidone/vinyl acetate (PVP/VA) copolymer, hydroxypropyl methylcellulose phthalate (HPMCP), hydroxypropyl methylcellulose acetate succinate (HPMCAS), and poly(methyl methacrylate) (PMMA). Both experiment and molecular dynamics simulation reveal diverse mixing behavior amongst the set of polymers. Detailed structural and nano-scale interaction analyses suggest that positive deviations from ideal-mixing behavior arise from the formation of stable polymer-CBD hydrogen

bonds whereas negative deviations are associated with disruptions to the polymer-polymer hydrogen-bond network. Polymer-water interaction analyses indicate the significance of polymer hydrophobicity that can lead to poor dissolution of CBD. These results have implications for drug dissolution rates based on how CBD and water interacts with each polymer. Furthermore, these insights may be used to guide ASD formulations for CBD or other small-molecule therapeutic agents.

1 Introduction

Cannabidiol (CBD) has garnered attention as a potential therapy for inflammation,[1–4] cancer,[5,6] and anxiety,[7–9] amongst other diseases and disorders, by targeting various signaling receptors and pathways.[10] Despite a global market size estimated to reach $20 billion by 2025,[11] the efficacy of CBD is limited by its solubility and bioavailability. With a water solubility of 12.6 mg/L[12] and lipophilicity (logP) of 6.3,[13] CBD is classified as a Biopharmaceutics Classification System (BCS) Class II drug.[14] Poor water solubility, along with a significant first-pass effect,[15] results in a low oral bioavailability of approximately 6%,[16] indicating that only a small portion of the drug reaches the circulatory system. Improvements to stabilization and controlled delivery methods for CBD could enhance the viability of certain treatments.

Amorphous solid dispersions (ASDs) enhance the solubility[17] and extend the shelf life[18–21] of active pharmaceutical ingredients (APIs) by mixing with a glassy polymer matrix.[22,23] The performance and stability of ASDs depend on polymer-API interactions that impact mixing behavior and subsequent dissolution.[24,25] Therefore, understanding how polymer chemistry influences API interactions is valuable for developing ASDs.

Numerous studies feature MD simulations to model the behavior of various ASDs. These studies often focus on predicting the solubility and Flory-Huggins interaction parameters of polymer-API systems at the macroscopic level.[26–36] Other studies utilize simulations to model formation of polymer-API matrices, mechanics of API dissolution, and hydration

effects within ASDs.[36–39] While MD simulations can be used to probe nanoscale interactions not accessible by experimental methods, studies utilizing MD to assess atomic-level behavior in ASDs have been limited to recent years.[27,40–42]

In this study, we combine molecular dynamics (MD) simulations and experimental characterizations to investigate CBD-polymer interactions in ASDs featuring several polymers: polyvinylpyrrolidone (PVP), polyvinylpyrrolidone/vinyl acetate (PVP/VA) copolymer, hydroxypropyl methylcellulose phthalate (HPMCP), hydroxypropyl methylcellulose acetate succinate (HPMCAS), and poly(methyl methacrylate) (PMMA) (Figure 1). Both experimental and simulated glass transition temperatures for ASDs across a range of compositions reveal system-specific mixing behavior with both positive and negative deviations from ideal-solution behavior observed. This behavior is elucidated through simulation analyses of the nanoscale structure of the polymer matrices and hydrogen-bonding characteristics within the ASDs. The distinct dissolution trends are further related to competition between CBD and water interactions with the polymer matrices. This complementary experimental and theoretical approach sheds light on the specific chemical moieties and molecular-level interactions that govern the mixing behavior of ASDs containing CBD. The analyses and insights supplied can help rationalize performance of ASDs containing CBD and may also facilitate design of other drug-delivery systems.

2 Methods

2.1 Experiment

Materials. Crystalline cannabidiol (CBD, 99.9%) was purchased from Global Cannabinoids (Las Vegas, NV). Hydroxypropyl methylcellulose acetate succinate (HPMCAS; Affinisol 126) was provided by the Dow Chemical Company (Midland, MI). Hydroxypropyl methylcellulose phthalate (HPMCP; HP-50) was provided by Shin-Etsu Chemical Co. (Tokyo, Japan). Polyvinylpyrrolidone (PVP; Kollidon 30) and polyvinylpyrrolidone-vinyl acetate copolymer

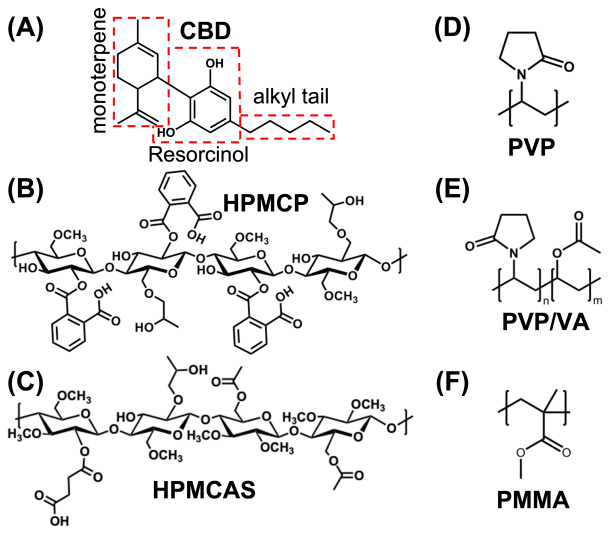

Figure 1: Overview of studied systems. Chemical structures and naming convention for (A) cannabidiol (CBD), (B) hydroxypropyl methylcellulose phthalate (HPMCP), (C) hydroxypropyl methylcellulose acetate succinate (HPMCAS), (D) polyvinylpyrrolidone (PVP), (E) polyvinylpyrrolidone-co-vinyl acetate (PVP/VA), and (F) poly(methyl methacrylate) (PMMA). For analysis, CBD is decomposed into a monoterpene, hydrophilic resorcinol, and the hydrophobic alkyl tail as shown in panel (A).

(PVP/VA; Kollidon VA 64) were provided by BASF Corporation (Tarrytown, NY). PVP/VA has an approximate 1.2:1 molar ratio of N-vinylpyrrolidone to vinyl acetate. Poly(methyl methacrylate) (PMMA) was purchased from Sigma-Aldrich (St. Louis, MO). Properties of polymers used are included in Supplemental Information, Table S1. Dichloromethane (DCM, HPLC grade), methanol (MeOH, HPLC grade), sodium hydroxide, tetrahydrofuran (THF, HPLC grade), acetonitrile (HPLC grade), and trifluoroacetic acid were purchased from Fisher Scientific (Hampton, NH). Fed-state Simulated Intestinal Fluid (FeSSIF V2) powder was purchased from Biorelevent.com, Ltd. (London, UK). Syringe filters (13 mm diameter, glass fiber, 0.45 µm pore size) were purchased from Foxx Life Sciences (Londonderry, NH). Tzero aluminum differential scanning calorimetry (DSC) pans (40 µL volume) and hermetic lids were purchased from TA Instruments (New Castle, DE). All materials were used without further purification.

Preparation of dropcast samples. Stock solutions were prepared for each CBD and polymer pairing, except for PMMA, at a concentration of 50 mg/mL in a 1:1 volumetric

mixture of DCM to MeOH. For pairng CBD with PMMA, dissolution was done in pure DCM. The solutions were volumetrically mixed to obtain desired CBD weight fractions $w_{\mathrm{CBD}} = m_{\mathrm{CBD}}/(m_{\mathrm{CBD}} + m_{\mathrm{polymer}}) = 0$, 0.2, 0.4, 0.6, 0.8, and 1.0. Each solution was added to a pre-weighed TA Tzero aluminum DSC pan in aliquots of 30 µL. Time was allowed for solvent evaporation under ambient conditions between each aliquot. Following the final aliquot, all pans were dried overnight in a vacuum oven at 30°C and -30 mmHg gauge pressure. Approximately five total solution aliquots were added to each pan to achieve a final solids mass of approximately 3–6 mg. Samples were prepared in triplicate and characterized by DSC.

Preparation of spray-dried ASDs containing CBD. Samples containing 20% CBD were prepared as spray-dried amorphous solid dispersions. Solutions were prepared at a total solid concentration of 5% w/w with $w_{\mathrm{CBD}} = 0.2$, in a 1:1 volumetric mixture of DCM to MeOH. Samples (10–20 mL) were spray dried using a B-290 spray dryer (Büchi Corporation, New Castle, DE) under nitrogen atmosphere in closed mode with a B-295 inert loop with $T_{\mathrm{condenser}}$ = -20°C for solvent recovery. The following parameters were used for spray drying: T_{inlet} = 90°C, T_{outlet} = 30–40°C, solution feed rate = 7 mL/min. The solution feed was atomized through a 0.7 mm diameter atomizing nozzle with nitrogen used as the atomizing gas (N_2 flow rate 470 L/h). The aspirator was set to a value of 90%, corresponding to a drying gas circulation rate of approximately 35 m^3/h. After spray drying, powders underwent an overnight secondary vacuum drying step (P_{gauge} = -30 mmHg) at room temperature for further removal of residual solvent. Samples were characterized by DSC, powder X-ray diffraction (PXRD), and in vitro release measurements.

Differential scanning calorimetry (DSC). Dropcast samples and spray-dried dispersions were thermally characterized by DSC. Approximately 3 – 5 mg of dropcast solids (after solvent evaporation) or 5 – 10 mg of powder was loaded into an aluminum DSC pan with

hermetic lid. A small pinhole was made in the pan lid to allow the escape of residual vapors. Characterization was performed using a TA Instruments Discovery 2500 DSC (New Castle, DE). Each sample was analyzed at a rate of 5°C/min over three heating and cooling cycles from -50 to 160°C, except for samples containing PVP, for which a temperature range of -50 to 190°C was used due to the elevated glass transition temperature of pure PVP. Data analysis was carried out using TA Universal Analysis software. The glass transition temperature is reported on second heating using the midpoint method. All heating cycles were monitored for evidence of potential phase separation (i.e. the presence of two distinct glass transition temperatures).

Powder X-ray diffraction (PXRD). PXRD measurements were performed using a D8 Advance twin diffractometer (Bruker Corporation, Billerica, MA) equipped with Cu Kα radiation (λ = 1.54 Å) and LYNXEYE-XE detector. Powder was loaded into a polyimide capillary (inner diameter = 1 mm), which was then mounted on a rotating (60 rpm) capillary stage. Data was collected in the range of 2θ = 3 - 20° with a step size of 0.025° and count rate of 5 s per step. Analysis was performed using Bruker DIFFRAC EVA V3.1 software. Additionally, for neat PMMA, CBD, and CBD-PMMA spray-dried ASDs, room-temperature Wide-angle X-ray Scattering (WAXS) was performed using a Xenocs Xeuss 3.0 (Xenocs, Holyoke, MA) equipped with a Cu Kα beamline. The samples were loaded into polyimide capillaries with the same inner diameter and mounted onto a stationary capillary stage. WAXS data were collected for 10 min per sample in the range of 2θ = 3 - 55°. The raw two-dimensional scattering data were azimuthally integrated to produce one-dimensional scattering patterns using the accompanying XSAFT software.

in vitro dissolution assay. The dissolution of CBD from spray-dried dispersions was measured using an in vitro assay in fed-state simulated intestinal fluid (FeSSIF). FeSSIF media was at pH 7 so as to be above the pKa of the functionalized cellulose polymers (rather

than pH 5.8) but otherwise according to the manufacturer's instructions. The FeSSIF media was pre-warmed in a 37°C water bath and then added to measured amounts of spray-dried dispersion powder to achieve a final CBD concentration of 200 µg/mL and a total liquid volume of approximately 10 mL.

To quantify the dissolution of CBD over time, a 0.25 mL aliquot of the release media was removed at 0.02, 0.25, 0.5, 1, 3, 6, and 24 hr. The aliquot was passed through a 0.45 µm glass fiber syringe filter (13 mm diameter) and was diluted five-fold with acetonitrile for HPLC analysis. For polymers other than PMMA, three separate aliquots of dissolution media taken from a single, larger vial of of the release media were taken at every time point to assess statistical variability. For PMMA, testing was done in full triplicate using three distinct vials of dissolution media. The two methods described are both expected to yield representative samples given the scale of spray dried samples.

High-performance Liquid Chromatograph (HPLC). CBD concentration was quantified by reverse-phase HPLC (Phenomenex Kinetex C18, 100 Å, 150 x 4.6 mm, 5 µm particles) using an Agilent 1100 series HPLC. Samples (10 µL injection volume) were analyzed with an isocratic mobile phase of 80:20 acetonitrile:water with 0.05% v/v trifluoroacetic acid at a flow rate of 1 mL/min and column temperature of 35°C. A diode array detector was used to detect CBD at a UV absorbance of 220 nm. The retention time was 3.7 minutes, and a linear standard curve was constructed for concentrations between 0.5–300 µg/mL using the integrated area of the UV absorbance peak. Samples were diluted with acetonitrile or mobile phase to fall within the range of the standard curve as needed.

2.2 Simulation

General Simulation Protocols. All MD simulations were performed using the GPU implementation of the OpenMM 7.7.0 simulation package.[43] The systems were modeled with the all-atom optimized potentials for liquid simulations (OPLS-AA) force field[44] with the

real-space non-bonded interactions truncated at 11 Å. Long-range electrostatics were calculated using the Particle Mesh Ewald (PME) algorithm, and long range energy corrections were applied for Lennard-Jones interactions beyond the cutoff range. Isothermal-isobaric simulations used a timestep of 1 fs, a Langevin thermostat integrator with a friction coefficient of 1 ps^{-1}, and a Monte Carlo barostat with a frequency of 25 fs. For each ASD, four independent simulations of five different CBD compositions were prepared, resulting in a total of $5 \times 5 \times 4 = 100$ simulations.

System Preparation. For each simulation, the number of polymer chains and CBD molecules were determined through a convex optimization procedure with system size constraints, as detailed in the Supplemental Information, Section 3. Using the CVXPY Python library[45,46] (version 1.4), molecule counts were calculated to maximize the accuracy of the resulting system mass concentrations while keeping the total atom count within a set range. The initial box size was chosen to obtain 90% of the pure polymer density. The polymer chains and CBD molecules were then placed randomly throughout the box at random orientations. The prepared systems were initially minimized using the OpenMM minimization algorithm with an energy tolerance of 1 kJ/mol, followed by velocity initialization at 373 K. The minimized structures were equilibrated in the isothermal-isobaric ensemble at 1 bar for 5 ns, followed by a 21-step compression/relaxation procedure (see Supplemental Information, Table S4) inspired by prior work.[47] The output configurations were then annealed from their respective target temperatures (Supplemental Information, Table S5) to 200 K at a rate of 10 K/ns with additional 2 ns equilibration every 10 K in the isothermal-isobaric ensemble at 1 bar. We note that the simulation times here are aggressive to equilibrate polymer systems of these molecular weights at these temperatures. An assessment of convergence of various properties is provided in the Supplemental Information, Figures S3-S6. Although the polymers are not likely equilibrated over all lengthscales, local structural properties, such as the density and various radial distribution functions, are effectively converged. Therefore, our

protocol seems adequate for the analysis herein.

Polymer Generation. Each polymer chain was built with 40 monomer units. To model the atacticity of PMMA, PVP, and PVP/VA, both isomers for each monomer were placed in the chains with equal probability. To model the substitution patterns in the cellulosic polymers, monomers with different substitutions were placed in the chains with probabilities matching the grades of polymers used in the experimental section. HP-50 HPMCP is approximately 22% w/w methoxy, 8% w/w hydroxypropoxy, and 24% w/w phthalyl.[48] Affinisol 126 HPMCAS is approximately 12% w/w acetyl, 6% w/w succinoyl, 24% w/w methoxyl, and 8% w/w hydroxypropoxy.[49] The hydroxypropyl polymer models were created based on a previous study.[36] Details for model monomer substitution patterns and distribution ratios are listed in Supplemental Information, Tables S2 and S3.

Glass Transition Temperatures. For density calculations to obtain T_g, 5 ns production simulations were run using the equilibrated configurations every 10 K with densities recorded every 1 ps. Estimates of T_g were formulated by using the densities at each temperature in the broken-stick model via statistically robust bootstrapping.[50,51] Two temperature ranges were manually specified around the expected T_g (Supplemental Information, Figure S2) and a best-fit line within each range was fitted with the bound of the range as the starting point and a randomly chosen end-point within the range. The temperature at which the two best-fit lines intersect was included in the final average T_g if it fell within the described bounds. A total of 5,000 iterations with randomly chosen end-points were repeated with the average denoting the calculated T_g for the system.

Structural Properties. The equilibrated configurations from the T_g simulations were further simulated for 30 ns in the isothermal-isobaric ensemble at 1 bar, and the configurations were saved every 10 ps. The simulations were performed at 310 K, approximately the human body temperature that is relevant for therapeutic applications. Radial distribution

functions (RDFs) were computed based on the distance between the centers of mass of the monomer units and two CBD groups, the hydrophilic resorcinol group and the hydrophobic alkyl tail. MDTraj Python library[52] (version 1.9.7.) was used to process the trajectories and generate the RDFs using histograms with a bin width of 0.1 Å.

Hydrogen-Bond Analysis. The hydrogen-bond counts were computed using the MDAnalysis Python library[53,54] (version 2.1.0) with hydrogen bonds defined geometrically with a cutoff angle of 150° and a cutoff distance of 3.5 Å over the same configurations as the previous section. The average polymer hydrogen-bond counts per volume (n_{HB}) were defined as the average number of hydrogen bonds that contain a polymer atom per frame divided by the average box volume in nm^3. The cohesive energy densities due to hydrogen bonding were calculated using[55]

$$e_{\mathrm{HB,IM}} = \frac{\Delta e_{\mathrm{vap,HB}}}{v} \tag{1}$$

where v is the molar volume of the system and $\Delta e_{\mathrm{vap,HB}}$ is the molar heat of vaporization from hydrogen-bond contributions, calculated using

$$\Delta e_{\mathrm{vap,HB}} = \sum_{i=1}^{N_{\mathrm{molecule}}} e_{i,\mathrm{HB}} - e_{\mathrm{liq,HB}} \tag{2}$$

where $e_{\mathrm{i,HB}}$ is the sum of pairwise hydrogen-bond energies within the i^{th} molecule in isolation and $e_{\mathrm{liq,HB}}$ is the total pairwise hydrogen-bond energy in the liquid system with periodic boundary conditions applied, computed every 3 ns for a total of 10 frames per system. Polymer hydrogen bonds were further categorized by their participating partner (polymer or CBD). The groups with an average of more than one hydrogen bond per frame at $w_{\mathrm{CBD}} = 0.2$ were included in the visual analysis.

For dynamic hydrogen-bond lifetime analysis, the equilibrated configurations at 310 K were further simulated in the microcanonical ensemble for 100 ps where the configurations

were saved every 10 fs. For each analysis window, detected hydrogen bonds at the initial frame of the window, $h_{ij}(t_0)$, were tracked every frame for 50 ps to obtain $h_{ij}(t_0 + \tau)$. The hydrogen-bond autocorrelation function was then calculated for all hydrogen bonds within each group via

$$C_{\mathrm{HB}}(\tau) = \frac{\langle h_{ij}(t_0) \cdot h_{ij}(t_0 + \tau) \rangle}{\langle h_{ij}(t_0)^2 \rangle} \tag{3}$$

where $C_{\mathrm{HB}}(\tau)$ denotes the autocorrelation function and τ denotes the time after initial window frame ($\tau_{\max} = 50$ ps). The analysis was repeated with t_0 increments of 2.5 ps, totalling 21 iterations to obtain $C_{\mathrm{HB}}(\tau)$ for each group. The average fraction of hydrogen bonds that persist was calculated via

$$\bar{P}_{\Delta\tau}(\tau_0) = \frac{1}{\Delta\tau} \int_{\tau_0}^{\tau_0 + \Delta\tau} C_{\mathrm{HB}}(\tau) d\tau \tag{4}$$

where $\bar{P}_{\Delta\tau}(\tau_0)$ is the average hydrogen-bond recurrence probability, $\Delta\tau$ is the recurrence interval length, and τ_0 is the initial frame.

Polymer Hydrophobicity Analysis. The hydrophobicity of each polymer was characterized via rotational relaxation time analysis of water molecules near polymer surface.[56] The neat polymer from T_{g} simulation at 300 K was further equilibrated for 10 ns in a large, non-periodic box (L = 1,000 Å) with no long-range electrostatic interactions. The equilibrated polymer pellet was then placed in a box where atoms are at least 15 Å away from the boundaries to prevent interactions with their periodic images. The water molecules were placed within a grid outside the polymer pellet with random orientations. The number of water molecules was chosen to result in a polymer-water mixture density of 1 g/cm^3 within the initial box. The water-pellet systems were initially minimized using the OpenMM minimization algorithm with an energy tolerance of 10 kJ/mol, followed by velocity initialization at 300 K. The minimized structures were equilibrated in the isothermal-isobaric ensemble

at 1 bar for 10 ns with simulation settings described in *General Simulation Protocols*. The equilibrated configurations at 300 K were further simulated in the microcanonical ensemble for 100 ps where the configurations were saved every 10 fs.

The orientational autocorrelation functions for water molecules were characterized via[57]

$$C_{\text{ori}}(\tau) = \langle P_2[\mathbf{u}(t_0) \cdot \mathbf{u}(t_0 + \tau)] \rangle \tag{5}$$

where P_2 is the second Legendre polynomial, $\mathbf{u}$ is the unit vector of the average of two O-H bond vectors. The orientational autocorrelation functions were calculated for water populations based on their proximity to the nearest polymer heavy atom with a distance bin size of 1 Å. Each autocorrelation function was then fit to a biexponential function, $A_1 e^{-t/\tau_1} + A_2 e^{-t/\tau_2}$, and the rotational time constant for each population was calculated as $\tau_{\text{rot}} = A_1\tau_1 + A_2\tau_2$.

3 Results & Discussion

3.1 Relative Extents of Dissolution

To assess the performance of each ASD, we characterize CBD dissolution over time. Figure 2 displays a spectrum of chemically specific dissolution rates across all ASDs. Cellulosic polymer systems, HPMCP and HPMCAS, exhibit the most rapid and substantial amongst this set of polymers. In contrast, PVP and PVP/VA systems are relatively slower and yield less complete dissolution of CBD within 24 hours. Dissolution of CBD is the slowest and least complete in PMMA, resulting in a dissolution extent below 12% in 24 hours. Overall, the relative ordering of dissolution extents, with cellulosic polymers ranking higher than pyrollidone-containing polymers ranking higher than PMMA, suggests a clear role of functional chemistry for CBD dissolution from ASDs.

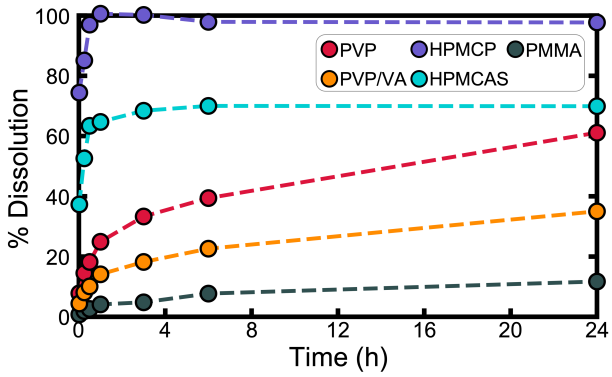

Figure 2: Overview of experimental dissolution trends across five amorphous solid dispersions. *In vitro* dissolution measurements for spray-dried dispersions of CBD with each polymer performed in FeSSIF at $w_{\mathrm{CBD}} = 0.2$.

3.2 Mixing Behavior Assessed through Composition-dependent Glass Transition Temperatures

We hypothesized that the relative extents of CBD dissolution could be explained by differences in enthalpic interactions between the polymer and CBD. Such differences could manifest in distinct mixing behaviors in the polymer-CBD ASDs. To initially assess mixing behavior, we examine the composition-dependence of glass transition temperatures, T_{g}. Glass transition temperatures of miscible multicomponent polymer systems often obey the Fox equation:[58]

$$\frac{1}{T_{\mathrm{g}}} = \sum_i \frac{w_i}{T_{\mathrm{g},i}} \tag{6}$$

where w_i denotes the mass fraction of component i and $T_{\mathrm{g},i}$ is the glass transition temperature for i as a pure substance. Eq. (6) presumes uniform and ideal mixing, such that certain properties (e.g., the specific volume and cohesive energy density) of the mixed system are simply additive combinations of the pure substances. Therefore, deviations from the Fox equation may reflect non-idealities related to the distribution or interaction of system components.

Figure 3A-E illustrates diverse mixing behaviors in polymer-CBD ASDs based on variation of T_{g} with increasing amounts of CBD. The simulated effective T_{g} appear systematically higher than corresponding experimental measurements, which we attribute to limitations of

simulated dilatometry.[51,59–61] Apart from this shift, both experiments and simulations show similar trends. ASDs with pyrrolidone-containing polymers (PVP and PVP/VA) exhibit positive deviations from the Fox equation (Figure 3A,B), those with cellulosic polymers (HPMCP and HPMCAS) display negative deviations (Figure 3C,D), and that with PMMA aligns with the Fox equation (Figure 3E).

Figure 3F indicates that the relative ordering of T_g values in experimental samples prepared via dropcasting or by spray-drying are also nearly identical. This may indicate that the nanoscale morphologies following either preparation protocol are similar or that the T_g trends are not remarkably sensitive to any morphological differences, suggesting minimal kinetic effects imparted by the processing technique. Because the simulations also necessarily adopt a different preparation protocol, these findings suggest the trends in T_g are robust across experimental and simulated systems.

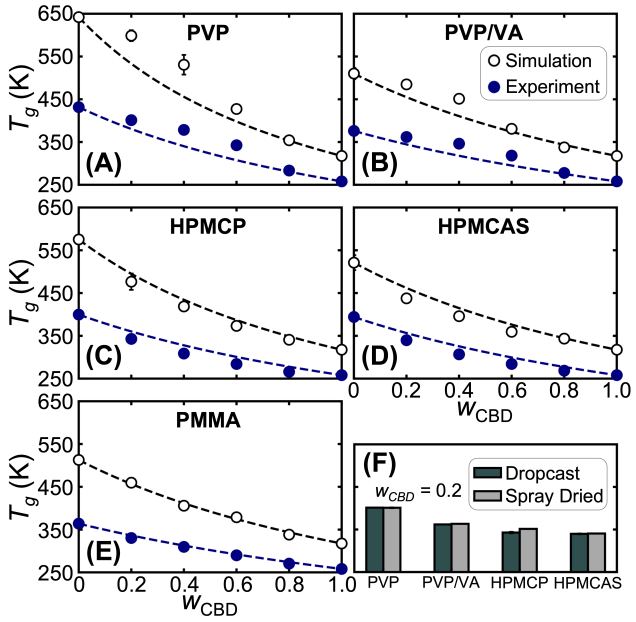

Figure 3: Comparison of glass transition temperatures across five amorphous solid dispersion systems. The experimental (via DSC of dropcast samples, navy) and computational (via MD, empty circles) glass transition temperatures are plotted against the weight fraction of CBD (with 0.2 increments) in polymer matrices containing (A) PVP, (B) PVP/VA, (C) HPMCP, (D) HPMCAS, and (E) PMMA. The data is compared against the Fox equation (dashed lines) representing the ideal mixing trends. (F) The comparison of T_g values obtained via dropcast and spray drying methods for PVP, PVP/VA, HPMCP and HPMCAS at a CBD weight fraction of 0.2. The error bars (black) in all panels represent the standard error of the mean from four independent trajectories and three experiment runs.

3.3 Relative Polymer-CBD Affinities Revealed by Nanoscale Morphology

Given the consistency between experimental and simulated trends, we now focus on analyzing the simulated systems to elucidate the chemical origins for differences in apparent mixing behavior. Figure 4A does not display any remarkable morphological differences that would suggest propensity for phase-separation or de-mixing based on simple visual inspection of simulated polymer-CBD configurations for each system. CBD molecules (green) appear mostly well-distributed throughout the polymer matrices. In simulations, finite-size effects could inhibit phase-separation;[62] however, experimental PXRD data (Supplemental Information, Figure S1) is also consistent with well-mixed amorphous systems.

Figure 4B-D do reveal minor differences in how CBD is distributed in ASDs at short ($<$ 1 nm) lengthscales. In particular, examining radial distribution functions (RDFs) between polymer atoms and different groups of the CBD (Figure 4B,C), cellulosic systems are distinguished by a lack of significant structuring of CBD at distances less than 8 Å whereas systems containing pyrrolidone feature slight enrichment of CBD, especially the resorcinol group, in proximity to polymer chains. The lack of structure in cellulosic systems is partly attributed to the relatively large size of the pendant groups on the constitutional units used for the RDF analysis. The local environment of CBD molecules is slightly enriched with other CBD molecules in cellulosic systems relative to those containing pyrrolidone (Figure 4D). The behavior of PMMA systems usually lies between the two other groups (most evident in Figure 4C).

Although systems appear macroscopically well-mixed in both simulation and experiment, the RDF analysis highlights structural trends that are reminiscent of the deviation trends for T_g in Figure 3. Amongst this set of polymers, PVP and PVP/VA showcase the strongest affinity for CBD, and these systems exhibit positive deviations from the Fox equation. Conversely, the structural signatures in cellulosic systems suggest relatively weaker affinity for CBD, and these systems exhibit negative deviations from the Fox equation. Last, PMMA is

an intermediate case, for which there was no notable deviation from the Fox equation.

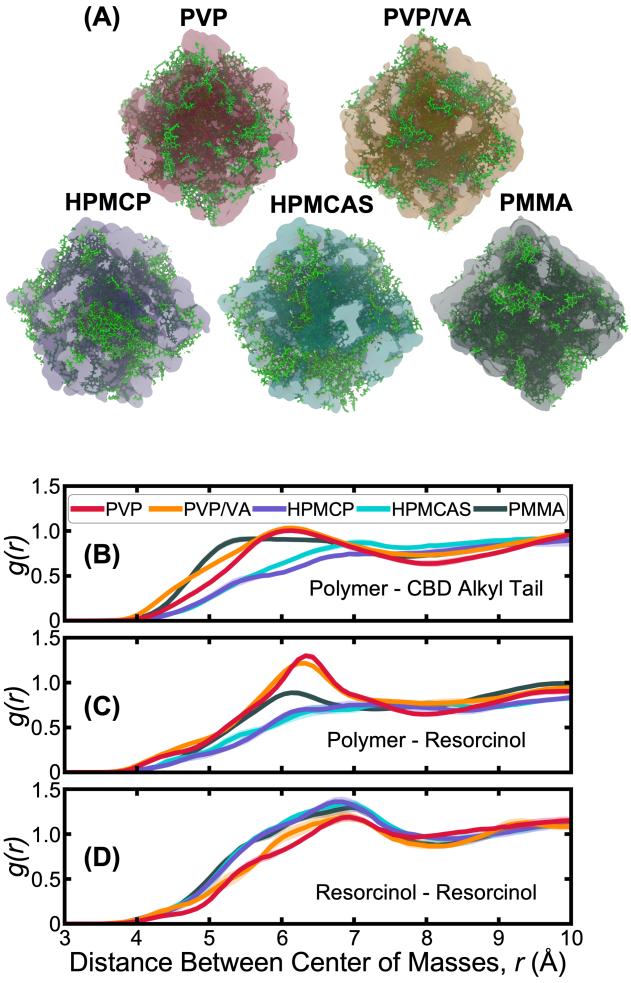

Figure 4: Overview of macromolecular structure of the simulated polymer-CBD matrices. (A) Snapshots visualizing each of the equilibrated simulation boxes at 310 K. The solid green structures represent the CBD molecules, the translucent regions represent the polymer chains and are shown in their respective colors throughout the study. Periodic boundary conditions are applied for all visuals. (B) Radial distribution functions (RDFs) between the pairs of monomer and CBD group centers of mass. The visualized groups include monomer-CBD alkyl group (top), monomer-CBD resorcinol group (middle), and CBD resorcinol pairs (bottom), obtained from 30 ns simulation trajectory at 310 K with a CBD weight fraction of 0.4. The standard error of the mean from four independent simulations are visualized as error regions for each RDF. Simulation visualizations of the equilibrated configurations were performed using the Visual Molecular Dynamics (VMD) software[63] (version 1.9.4).

3.4 Characterization of Composition-Dependent Hydrogen-Bonding Behaviors

To rationalize the apparent relative affinities for CBD in the various polymers, we examine the role of hydrogen-bonding. Figure 5 visualizes the hydrogen-bonding contributions

governing the observed mixing behavior within each system. Figure 5A tracks the overall number density of hydrogen bonds involving polymer atoms (either polymer-polymer or polymer-CBD hydrogen bonds), $n_{\mathrm{HB,polymer}}$, as a function of CBD concentration. The data again illustrates three contrasting sets of behavior between PMMA versus cellulosic polymers versus pyrrolidone-containing polymers. Starting with neat polymers, adding CBD to cellulosic polymers notably decreases $n_{\mathrm{HB,polymer}}$, while the extent of hydrogen-bonding increases in PMMA, PVP, and PVP/VA. The latter effect is somewhat trivial, as none of PVP, PVP/VA, or PMMA can form polymer-polymer hydrogen bonds because they lack hydrogen-bond donors; however, it is notable that the increase is more striking in PVP and PVP/VA compared to PMMA. By contrast, cellulosic polymers do form polymer-polymer hydrogen bonds with the implication that adding CBD disrupts such bonding without effective replacement with polymer-CBD bonds.

Figure 5B reveals similar trends through changes to the cohesive energy density due to hydrogen-bonding. Strikingly, the relative deviations from ideal expectations align well with the derivatives of these quantities with respect to CBD composition when CBD is the minority component. For example, $\left(\frac{\partial n_{\mathrm{HB,polymer}}}{\partial w_{\mathrm{CBD}}}\right)_{T,p}$ goes from negative for HPMCP and HPMCAS to weakly positive for PMMA to positive for PVP and PVP/VA, which is the same order of progression for deviations from the Fox equation. We note that cohesive energy densities are also commonly related to Hansen solubility parameters, which would seem to also be an intuitive metric for assessing dissolution and mixing. However, we do not find any obvious trends with total Hansen solubility parameters (Supplemental Information, Figure S7). Consequently, we conclude that distinct hydrogen-bonding behavior likely underlies the mixing trends observed across these ASDs.

3.5 Role of Functional Chemistry on Hydrogen-Bonding Behavior

To better understand the origin of the hydrogen-bonding trends in Figure 5, we analyze hydrogen-bond contributions from different functional groups in Figure 6. For cellulosic

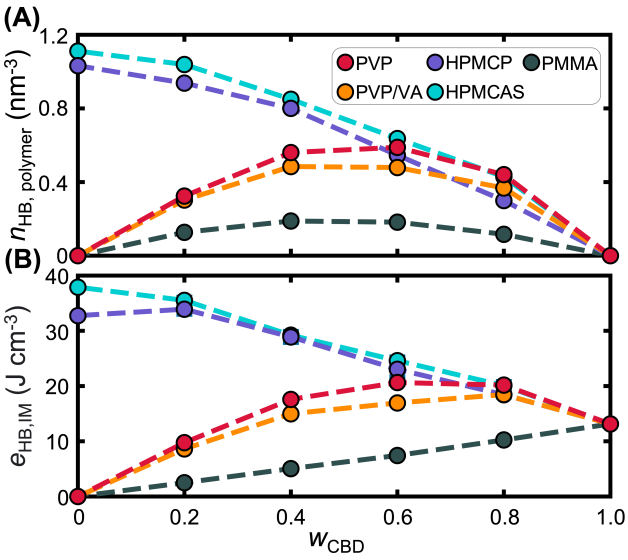

Figure 5: Overview of hydrogen-bonding contributions within various ASDs at 310 K. (A) Number of hydrogen bonds per unit volume involving at least one polymer atom varying with CBD composition. (B) Comparison of the cohesive energy densities due to hydrogen bonding from all hydrogen-bonding energy contributions in each polymer matrix. Error bars (black) represent the standard error of the mean from four independent trajectories of 30 ns and are not visible under the markers.

ASDs (Figure 6A,B), most hydrogen bonds involve hydroxyl groups positioned away from the polymer backbone. Tracking polymer-polymer and polymer-CBD hydrogen bonds with increasing CBD content reveals saturation of polymer-CBD contributions while polymer-polymer contributions diminish, explaining the net decrease in Figure 5A. In the remaining polymers, which possess fewer hydrogen-acceptor sites, the extent of positive deviation from the Fox equation correlates well with the total number of polymer-CBD hydrogen bonds. In PVP, such interactions are facilitated through the carbonyl group of the pyrrolidone (Figure 6C). The same is true for PVP/VA (Figure 6D), which implies that CBD possesses greater affinity to engage in hydrogen-bonding with the pyrollidone group compared to the acetate ester. Meanwhile, PMMA (Figure 6E) only engages in hydrogen-bonding through its acetate ester and features fewer overall hydrogen-bonding interactions relative to PVP/VA. Collectively, this analysis suggests that hydrogen-bonding between the carbonyl group of pyrrolidone and CBD is the predominant factor governing positive deviations with the Fox equation for PVP and PVP/VA, while the disruption of polymer-polymer hydrogen-bonds in cellulosic polymers underlies their negative deviations.

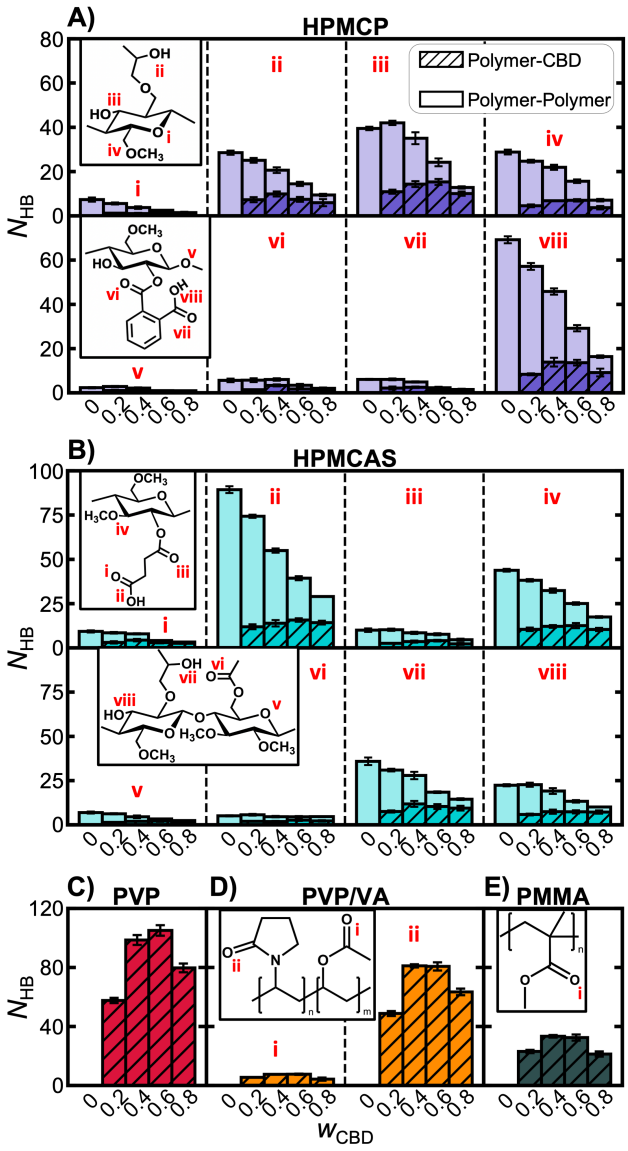

Figure 6: Breakdown of hydrogen-bond counts involving various polymer groups at 310 K. Oxygen atoms with at least one hydrogen bond per frame on average (at $w_{CBD} = 0.2$) are visualized for (A) HPMCP, (B) HPMCAS, (C) PVP, (D) PVP/VA, and (E) PMMA. Each plot corresponds to their respective oxygen atoms labeled in the inset chemical structures. Polymer hydrogen bonds are categorized based on the participant pairs where interactions with other polymer groups are displayed in solid color, and those with CBD molecules are displayed with hatching. As PVP only has one oxygen atom type, no explicit labeling is needed. Error bars (black) represent the standard error of the mean from four independent 30 ns trajectories.

3.6 Hydrogen-Bond Dynamics as a Proxy for Interaction Stability

To further understand implications of hydrogen-bonding on system dynamics, we characterize average hydrogen-bond recurrence probabilities $\bar{P}_{\Delta\tau}$ (see eq 4) across the different polymer-CBD ASDs. We interpret long-lived (high-recurrence) hydrogen bonds as being indicative of strong dynamic coupling and more likely slower dynamics whereas more frequent

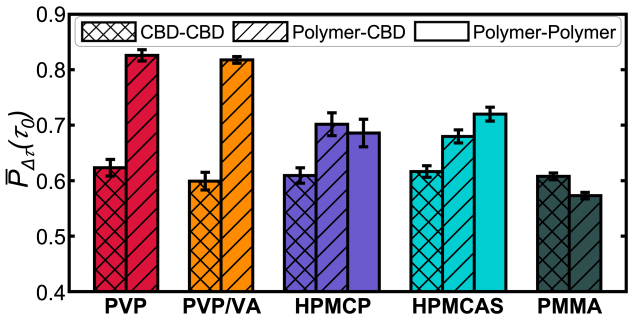

Figure 7: Overview of hydrogen-bond dynamics across five ASDs at $w_{\mathrm{CBD}} = 0.2$ at 310 K. The average hydrogen-bond recurrence probabilities $\bar{P}_{\Delta\tau}$ are plotted for each hydrogen-bond pair type within every polymer matrix for $\Delta\tau = \tau_0 = 25$ ps. The analyzed pair types include CBD-CBD (cross-hatching), polymer-CBD (forward-slash hatching), and polymer-polymer (solid). Error bars (black) represent the standard error of the mean from four independent 100 ps trajectories.

exchange of hydrogen-bonding partners implies more rapid molecular dynamics.

Figure 7 displays dynamic trends consistent with hydrogen-bonding contributions via comparison of recurrence probabilities for different hydrogen-bonding types across each ASD. Polymer-CBD hydrogen bonds are significantly more static than CBD-CBD hydrogen bonds, implying a strong dynamic coupling between these polymers and CBD. We suggest that the presence of the CBD molecules reduces polymer mobility by anchoring chains with stable hydrogen bonds, resulting in positive enhancements to T_{g} relative to the Fox equation. The remaining systems do not possess such stark contrast amongst hydrogen-bond types.

For cellulosic systems, polymer-polymer and polymer-CBD lifetimes are comparable. However, because lost polymer-polymer hydrogen bonds are not compensated for by longer-lived polymer-CBD hydrogen bonds, we conclude that the net reduction in hydrogen bonds involving polymer atoms governs the observed enhanced plasticization relative to the Fox equation. In PMMA, polymer-CBD hydrogen bonds are more dynamic than in PVP and PVP/VA. Furthermore, polymer-CBD and CBD-CBD hydrogen bonds are comparable in recurrence probability. This implies that the dynamic coupling between PMMA and CBD is similar to that of CBD with CBD, such that dynamic trends arise simply from concentration effects of CBD, consistent with the notion of ideal mixing. The relative dynamic stability of various hydrogen-bond types thus correlates well with observed mixing trends, which connect to observed dissolution rates.

3.7 Competing Effect of Polymer Hydrophobicity on Dissolution

The observed mixing and intermolecular interaction trends largely explain the dissolution behavior observed in various ASDs. However, the conclusions from experiment and simulation suggests that PMMA ASDs containing weak polymer-CBD interactions should have a high CBD dissolution rate, conflicting with the observation in Figure 2. The high water content of the FeSSIF dissolution media suggests that polymer hydrophobicity may play an important role in the dissolution mechanism. Rotational relaxation time of water molecules near polymer surfaces has been recently suggested as a measure of polymer nanoscale hydrophobicity.[56] High relaxation times indicate stronger polymer-water interactions that restrict the motion of water molecules, suggesting hydrophilicity. In contrast, fast orientational relaxation near polymer surface is observed due to the lack of strong forces acting on the water molecules by the polymer chain, suggesting hydrophobicity. We specifically examine the dynamics of water molecules within 8 Å of a solvated polymer pellet (Figure 8A).

Figure 8B highlights the importance of polymer hydrophobicity on dissolution behavior that cannot be explained purely by analysis of polymer-CBD interactions. The mean rotational relaxation times of water molecules as a function of distance from the nearest polymer for each system vary at low distances. PMMA displays the lowest relaxation times across all systems, indicating its high hydrophobicity. PVP and PVP/VA are the most hydrophilic of all systems, followed by the cellulosic polymer ASDs, HPMCP and HPMCAS. Comparison of dissolution and hydrophobicity trends show that polymer hydrophobicity alone does not explain the dissolution behavior. This suggests competing effects between polymer-CBD and polymer-water interactions on the extent of dissolution: polymers that form strong hydrogen bonds with the CBD molecules also strongly interact with water. In the case of PMMA, the effect of weak polymer-water interactions dominate that of weak polymer-CBD interactions, resulting in low CBD dissolution. Inclusion of polymer hydrophobicity provides a complete picture of the factors governing the observed dissolution behavior in which both polymer-water and polymer-API interactions play an important role.

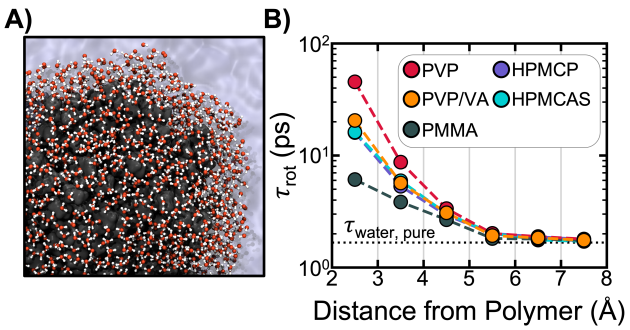

Figure 8: Characterization of polymer hydrophobicity via water dynamics surrounding solvated polymer pellets. (A) A representative simulation snapshot illustrating water molecules within 8 Å of any polymer atom. The specific system shown is for PVP. For explicitly represented waters, oxygen atoms are in red and hydrogen atoms are white. The polymer surface is depicted as a gray surface. The transparent blue surface highlights the presence of water molecules that are beyond the 8 Å threshold. (B) The relative rotational relaxation time constants for water molecules as a function of distance from various polymers. All data is for 300 K. Markers indicate the mean rotational relaxation time constants for water molecules that lie between two distance bounds (gray, solid lines) with distances based on the nearest heavy atom on the polymer. The black dotted line is a reference to the time constant obtained from a pure water simulation at 300 K. Error bars represent the standard error of the mean from four independent 100 ps trajectories and are generally smaller than the marker size.

4 Conclusions

We investigated polymer-CBD interactions that give rise to distinct mixing behaviors in a variety of ASDs. Experimental and computational findings reveal that PVP and PVP/VA exhibit positive deviations from ideal mixing behavior in contrast with the negative deviatons observed in the cellulosic systems, HPMCP and HPMCAS. The results also show that PMMA remains in line with ideal mixing predictions. Detailed analysis of the polymer matrix structures and hydrogen-bonding characteristics and dynamics elucidate the origins of specific mixing behavior. Distinct water dynamics trends from polymer-water simulations highlight the negative impact of polymer hydrophobicity that results in poor dissolution of CBD in the PMMA systems. We conclude that the distinct mixing behavior in the investigated ASDs is primarily governed by the distinct hydrogen-bond groups on the various polymers. Polymers containing hydrogen-bond donors form a stable polymer-polymer interaction network disrupted by the CBD molecules.

This study provides a deeper understanding regarding how polymer-API interactions, particularly polymer-CBD interactions, can affect mixing mixing trends in ASDs and dissolution rates. Polymers containing only hydrogen-bond acceptors display a net increase in the polymer-CBD hydrogen bonds that anchor the chains, resulting in a higher T_g than predicted

by the Fox equation. ASDs that weakly interact with the CBD molecules exhibit neither effect and follow the ideal mixing trends. Nevertheless, these mixing trends do not completely explain observed dissolution rates, which required additional consideration of hydrophobicity effects. These insights can inform the design of materials for drug-delivery in future pharmaceutical applications; however, the presence of competing effects renders outcomes difficult to anticipate. Nevertheless, the capability to elucidate experimental trends through the presented analyses provides a viable pathway for computationally guided formulation optimization. Future work may aim to understand how the relative importance and balance of polymer-API, polymer-water, and API-water interactions influence dissolution. In this, it may be interesting to consider whether this balance is a strong function of conditions, such as temperature or pH.

Acknowledgement

B.E.U. and M.A.W. acknowledge support from the National Science Foundation under Grant No. 2237470. Simulations and analyses were performed using resources from Princeton Research Computing at Princeton University, which is a consortium led by the Princeton Institute for Computational Science and Engineering (PICSciE) and Office of Information Technology's Research Computing. The authors acknowledge the use of Princeton's Imaging and Analysis Center (IAC), which is partially supported by the Princeton Center for Complex Materials (PCCM), a National Science Foundation (NSF) Materials Research Science and Engineering Center (MRSEC; DMR-2011750).

Supporting Information

Properties of Investigated Polymers. Powder X-ray Diffraction (PXRD) Measurements. Preparation of Initial Simulation Configurations. Simulation Settings. Analysis of Simulated Systems.

References

(1) Watt, G.; Karl, T. In vivo Evidence for Therapeutic Properties of Cannabidiol (CBD) for Alzheimer's Disease. *Frontiers in Pharmacology* **2017**, *8*, 20, DOI: 10.3389/fphar.2017.00020.

(2) Lunn, C. A.; Fine, J. S.; Rojas-Triana, A.; Jackson, J. V.; Fan, X.; Kung, T. T.; Gonsiorek, W.; Schwarz, M. A.; Lavey, B.; Kozlowski, J. A.; Narula, S. K.; Lundell, D. J.; Hipkin, R. W.; Bober, L. A. A Novel Cannabinoid Peripheral Cannabinoid Receptor-Selective Inverse Agonist Blocks Leukocyte Recruitment in Vivo. *Journal of Pharmacology and Experimental Therapeutics* **2005**, *316*, 780–788, DOI: 10.1124/jpet.105.093500.

(3) Malfait, A. M.; Gallily, R.; Sumariwalla, P. F.; Malik, A. S.; Andreakos, E.; Mechoulam, R.; Feldmann, M. The nonpsychoactive cannabis constituent cannabidiol is an oral anti-arthritic therapeutic in murine collagen-induced arthritis. *Proceedings of the National Academy of Sciences* **2000**, *97*, 9561–9566, DOI: 10.1073/pnas.160105897.

(4) Mecha, M.; Feliú, A.; Iñigo, P.; Mestre, L.; Carrillo-Salinas, F.; Guaza, C. Cannabidiol provides long-lasting protection against the deleterious effects of inflammation in a viral model of multiple sclerosis: A role for A2A receptors. *Neurobiology of Disease* **2013**, *59*, 141–150, DOI: 10.1016/j.nbd.2013.06.016.

(5) Guzmán, M. Cannabinoids: potential anticancer agents. *Nature Reviews Cancer* **2003**, *3*, 745–755, DOI: 10.1038/nrc1188.

(6) Salazar, M.; Lorente, M.; García-Taboada, E.; Hernández-Tiedra, S.; Davila, D.; Francis, S. E.; Guzmán, M.; Kiss-Toth, E.; Velasco, G. The pseudokinase tribbles homologue-3 plays a crucial role in cannabinoid anticancer action. *Biochimica et Biophysica Acta (BBA) - Molecular and Cell Biology of Lipids* **2013**, *1831*, 1573–1578, DOI: 10.1016/j.bbalip.2013.03.014.

(7) Bergamaschi, M. M.; Queiroz, R. H. C.; Chagas, M. H. N.; de Oliveira, D. C. G.; De Martinis, B. S.; Kapczinski, F.; Quevedo, J.; Roesler, R.; Schr oder, N.; Nardi, A. E.; Martín-Santos, R.; Hallak, J. E. C.; Zuardi, A. W.; Crippa, J. A. S. Cannabidiol Reduces the Anxiety Induced by Simulated Public Speaking in Treatment-Na ive Social Phobia Patients. *Neuropsychopharmacology* **2011**, *36*, 1219–1226, DOI: 10.1038/npp.2011.6.

(8) Mandolini, G. M.; Lazzaretti, M.; Pigoni, A.; Oldani, L.; Delvecchio, G.; Brambilla, P. Pharmacological properties of cannabidiol in the treatment of psychiatric disorders: a critical overview. *Epidemiology and Psychiatric Sciences* **2018**, *27*, 327–335, DOI: 10.1017/s2045796018000239.

(9) Rey, A. A.; Purrio, M.; Viveros, M.-P.; Lutz, B. Biphasic Effects of Cannabinoids in Anxiety Responses: CB1 and GABAB Receptors in the Balance of GABAergic and Glutamatergic Neurotransmission. *Neuropsychopharmacology* **2012**, *37*, 2624–2634, DOI: 10.1038/npp.2012.123.

(10) White, C. M. A Review of Human Studies Assessing Cannabidiol's (CBD) Therapeutic Actions and Potential. *The Journal of Clinical Pharmacology* **2019**, *59*, 923–934, DOI: 10.1002/jcph.1387.

(11) Villanueva, M. R. B.; Joshaghani, N.; Villa, N.; Badla, O.; Goit, R.; Saddik, S. E.; Dawood, S. N.; Rabih, A. M.; Niaj, A.; Raman, A.; Uprety, M.; Calero, M.; Khan, S. Efficacy, Safety, and Regulation of Cannabidiol on Chronic Pain: A Systematic Review. *Cureus* **2022**, e26913, DOI: 10.7759/cureus.26913.

(12) Pagano, S.; Coniglio, M.; Valenti, C.; Federici, M. I.; Lombardo, G.; Cianetti, S.; Marinucci, L. Biological effects of Cannabidiol on normal human healthy cell populations: Systematic review of the literature. *Biomedicine &; Pharmacotherapy* **2020**, *132*, 110728, DOI: 10.1016/j.biopha.2020.110728.

(13) Stella, B.; Baratta, F.; Della Pepa, C.; Arpicco, S.; Gastaldi, D.; Dosio, F. Cannabinoid Formulations and Delivery Systems: Current and Future Options to Treat Pain. *Drugs* **2021**, *81*, 1513–1557, DOI: 10.1007/s40265-021-01579-x.

(14) Grifoni, L.; Vanti, G.; Donato, R.; Sacco, C.; Bilia, A. R. Promising Nanocarriers to Enhance Solubility and Bioavailability of Cannabidiol for a Plethora of Therapeutic Opportunities. *Molecules* **2022**, *27*, 6070, DOI: 10.3390/molecules27186070.

(15) Millar, S. A.; Stone, N. L.; Yates, A. S.; O'Sullivan, S. E. A Systematic Review on the Pharmacokinetics of Cannabidiol in Humans. *Frontiers in Pharmacology* **2018**, *9*, 1365, DOI: 10.3389/fphar.2018.01365.

(16) Gaston, T. E.; Friedman, D. Pharmacology of cannabinoids in the treatment of epilepsy. *Epilepsy & Behavior* **2017**, *70*, 313–318, DOI: 10.1016/j.yebeh.2016.11.016.

(17) Newman, A.; Knipp, G.; Zografi, G. Assessing the performance of amorphous solid dispersions. *Journal of Pharmaceutical Sciences* **2012**, *101*, 1355–1377, DOI: 10.1002/jps.23031.

(18) Blass, B. The Characterization of Cannabidiol Amorphous Solid Dispersions. mathesis, Arizona State University, 2019.

(19) Sahoo, A.; Suryanarayanan, R.; Siegel, R. A. Stabilization of Amorphous Drugs by Polymers: The Role of Overlap Concentration (C*). *Molecular Pharmaceutics* **2020**, *17*, 4401–4406, DOI: 10.1021/acs.molpharmaceut.0c00576.

(20) Duarte, Í.; Santos, J. L.; Pinto, J. F.; Temtem, M. Screening Methodologies for the Development of Spray-Dried Amorphous Solid Dispersions. *Pharmaceutical Research* **2014**, *32*, 222–237, DOI: 10.1007/s11095-014-1457-5.

(21) Sun, Y.; Zhu, L.; Wu, T.; Cai, T.; Gunn, E. M.; Yu, L. Stability of Amorphous Phar-

maceutical Solids: Crystal Growth Mechanisms and Effect of Polymer Additives. *The AAPS Journal* **2012**, *14*, 380–388, DOI: 10.1208/s12248-012-9345-6.

(22) Pandi, P.; Bulusu, R.; Kommineni, N.; Khan, W.; Singh, M. Amorphous solid dispersions: An update for preparation, characterization, mechanism on bioavailability, stability, regulatory considerations and marketed products. *International Journal of Pharmaceutics* **2020**, *586*, 119560, DOI: 10.1016/j.ijpharm.2020.119560.

(23) Rawlinson, C. F.; Williams, A. C.; Timmins, P.; Grimsey, I. Polymer-mediated disruption of drug crystallinity. *International Journal of Pharmaceutics* **2007**, *336*, 42–48, DOI: 10.1016/j.ijpharm.2006.11.029.

(24) Li, N.; Taylor, L. S. Tailoring supersaturation from amorphous solid dispersions. *Journal of Controlled Release* **2018**, *279*, 114–125, DOI: 10.1016/j.jconrel.2018.04.014.

(25) Ohara, T.; Kitamura, S.; Kitagawa, T.; Terada, K. Dissolution mechanism of poorly water-soluble drug from extended release solid dispersion system with ethylcellulose and hydroxypropylmethylcellulose. *International Journal of Pharmaceutics* **2005**, *302*, 95–102, DOI: 10.1016/j.ijpharm.2005.06.019.

(26) Gupta, J.; Nunes, C.; Vyas, S.; Jonnalagadda, S. Prediction of Solubility Parameters and Miscibility of Pharmaceutical Compounds by Molecular Dynamics Simulations. *The Journal of Physical Chemistry B* **2011**, *115*, 2014–2023, DOI: 10.1021/jp108540n.

(27) Yani, Y.; Kanaujia, P.; Chow, P. S.; Tan, R. B. H. Effect of API-Polymer Miscibility and Interaction on the Stabilization of Amorphous Solid Dispersion: A Molecular Simulation Study. *Industrial &; Engineering Chemistry Research* **2017**, *56*, 12698–12707, DOI: 10.1021/acs.iecr.7b03187.

(28) Barmpalexis, P.; Karagianni, A.; Katopodis, K.; Vardaka, E.; Kachrimanis, K. Molecular modelling and simulation of fusion-based amorphous drug dispersions in poly-

mer/plasticizer blends. *European Journal of Pharmaceutical Sciences* **2019**, *130*, 260–268, DOI: 10.1016/j.ejps.2019.02.004.

(29) Iesavand, H.; Rahmati, M.; Afzali, D.; Modiri, S. Investigation on absorption and release of mercaptopurine anticancer drug from modified polylactic acid as polymer carrier by molecular dynamic simulation. *Materials Science and Engineering: C* **2019**, *105*, 110010, DOI: 10.1016/j.msec.2019.110010.

(30) Xiang, T.-X.; Anderson, B. D. Molecular Dynamics Simulation of Amorphous Indomethacin-Poly(Vinylpyrrolidone) Glasses: Solubility and Hydrogen Bonding Interactions. *Journal of Pharmaceutical Sciences* **2013**, *102*, 876–891, DOI: 10.1002/jps.23353.

(31) Xiang, T.-X.; Anderson, B. D. Molecular Dynamics Simulation of Amorphous Hydroxypropylmethylcellulose and Its Mixtures With Felodipine and Water. *Journal of Pharmaceutical Sciences* **2017**, *106*, 803–816, DOI: 10.1016/j.xphs.2016.10.026.

(32) Kapourani, A.; Chatzitheodoridou, M.; Kontogiannopoulos, K. N.; Barmpalexis, P. Experimental, Thermodynamic, and Molecular Modeling Evaluation of Amorphous Simvastatin-Poly(vinylpyrrolidone) Solid Dispersions. *Molecular Pharmaceutics* **2020**, *17*, 2703–2720, DOI: 10.1021/acs.molpharmaceut.0c00413.

(33) Macháčková, M.; Tokarský, J.; fåapková, P. A simple molecular modeling method for the characterization of polymeric drug carriers. *European Journal of Pharmaceutical Sciences* **2013**, *48*, 316–322, DOI: 10.1016/j.ejps.2012.11.010.

(34) Eslami, M.; Nikkhah, S. J.; Hashemianzadeh, S. M.; Sajadi, S. A. S. The compatibility of Tacrine molecule with poly(n-butylcyanoacrylate) and Chitosan as efficient carriers for drug delivery: A molecular dynamics study. *European Journal of Pharmaceutical Sciences* **2016**, *82*, 79–85, DOI: 10.1016/j.ejps.2015.11.014.

(35) Brunsteiner, M.; Khinast, J.; Paudel, A. Relative Contributions of Solubility and Mobility to the Stability of Amorphous Solid Dispersions of Poorly Soluble Drugs: A Molecular Dynamics Simulation Study. *Pharmaceutics* **2018**, *10*, 101, DOI: 10.3390/pharmaceutics10030101.

(36) Jha, P. K.; Larson, R. G. Assessing the Efficiency of Polymeric Excipients by Atomistic Molecular Dynamics Simulations. *Molecular Pharmaceutics* **2014**, *11*, 1676–1686, DOI: 10.1021/mp500068w.

(37) Chan, T.; Ouyang, D. Investigating the molecular dissolution process of binary solid dispersions by molecular dynamics simulations. *Asian Journal of Pharmaceutical Sciences* **2018**, *13*, 248–254, DOI: 10.1016/j.ajps.2017.07.011.

(38) Han, R.; Huang, T.; Liu, X.; Yin, X.; Li, H.; Lu, J.; Ji, Y.; Sun, H.; Ouyang, D. Insight into the Dissolution Molecular Mechanism of Ternary Solid Dispersions by Combined Experiments and Molecular Simulations. *AAPS PharmSciTech* **2019**, *20*, 274, DOI: 10.1208/s12249-019-1486-9.

(39) Razmimanesh, F.; Amjad-Iranagh, S.; Modarress, H. Molecular dynamics simulation study of chitosan and gemcitabine as a drug delivery system. *Journal of Molecular Modeling* **2015**, *21*, 165, DOI: 10.1007/s00894-015-2705-2.

(40) Cadden, J.; Gupta, K. M.; Kanaujia, P.; Coles, S. J.; Aitipamula, S. Cocrystal Formulations: Evaluation of the Impact of Excipients on Dissolution by Molecular Simulation and Experimental Approaches. *Crystal Growth &; Design* **2020**, *21*, 1006–1018, DOI: 10.1021/acs.cgd.0c01351.

(41) Zhang, M.; Huang, Y.; Hao, D.; Ji, Y.; Ouyang, D. Solvation structure and molecular interactions of ibuprofen with ethanol and water: A theoretical study. *Fluid Phase Equilibria* **2020**, *510*, 112454, DOI: 10.1016/j.fluid.2019.112454.

(42) Lu, X.; Li, M.; Huang, C.; Lowinger, M. B.; Xu, W.; Yu, L.; Byrn, S. R.; Templeton, A. C.; Su, Y. Atomic-Level Drug Substance and Polymer Interaction in Posaconazole Amorphous Solid Dispersion from Solid-State NMR. *Molecular Pharmaceutics* **2020**, *17*, 2585–2598, DOI: 10.1021/acs.molpharmaceut.0c00268.

(43) Eastman, P.; Swails, J.; Chodera, J. D.; McGibbon, R. T.; Zhao, Y.; Beauchamp, K. A.; Wang, L.-P.; Simmonett, A. C.; Harrigan, M. P.; Stern, C. D.; Wiewiora, R. P.; Brooks, B. R.; Pande, V. S. OpenMM 7: Rapid development of high performance algorithms for molecular dynamics. *PLOS Computational Biology* **2017**, *13*, e1005659, DOI: 10.1371/journal.pcbi.1005659.

(44) Jorgensen, W. L.; Maxwell, D. S.; Tirado-Rives, J. Development and Testing of the OPLS All-Atom Force Field on Conformational Energetics and Properties of Organic Liquids. *Journal of the American Chemical Society* **1996**, *118*, 11225–11236, DOI: 10.1021/ja9621760.

(45) Diamond, S.; Boyd, S. CVXPY: A Python-Embedded Modeling Language for Convex Optimization. 2016.

(46) Agrawal, A.; Verschueren, R.; Diamond, S.; Boyd, S. A rewriting system for convex optimization problems. *Journal of Control and Decision* **2018**, *5*, 42–60, DOI: 10.1080/23307706.2017.1397554.

(47) Larsen, G. S.; Lin, P.; Hart, K. E.; Colina, C. M. Molecular Simulations of PIM-1-like Polymers of Intrinsic Microporosity. *Macromolecules* **2011**, *44*, 6944–6951, DOI: 10.1021/ma200345v.

(48) Fukasawa, M.; Obara, S. Molecular Weight Determination of Hypromellose Phthalate (HPMCP) Using Size Exclusion Chromatography with a Multi-angle Laser Light Scattering Detector. *Chemical and Pharmaceutical Bulletin* **2003**, *51*, 1304–1306, DOI: 10.1248/cpb.51.1304.

(49) Fukasawa, M.; Obara, S. Molecular Weight Determination of Hypromellose Acetate Succinate (HPMCAS) Using Size Exclusion Chromatography with a Multi-Angle Laser Light Scattering Detector. *Chemical and Pharmaceutical Bulletin* **2004**, *52*, 1391–1393, DOI: 10.1248/cpb.52.1391.

(50) Deng, C.; Webb, M. A.; Bennington, P.; Sharon, D.; Nealey, P. F.; Patel, S. N.; de Pablo, J. J. Role of Molecular Architecture on Ion Transport in Ethylene oxide-Based Polymer Electrolytes. *Macromolecules* **2021**, *54*, 2266–2276, DOI: 10.1021/acs.macromol.0c02424.

(51) Chu, W.; Webb, M. A.; Deng, C.; Colón, Y. J.; Kambe, Y.; Krishnan, S.; Nealey, P. F.; de Pablo, J. J. Understanding Ion Mobility in P2VP/$NMP^{+}I^{-}$ Polymer Electrolytes: A Combined Simulation and Experimental Study. *Macromolecules* **2020**, *53*, 2783–2792, DOI: 10.1021/acs.macromol.9b02329.

(52) McGibbon, R.; Beauchamp, K.; Harrigan, M.; Klein, C.; Swails, J.; Hernández, C.; Schwantes, C.; Wang, L.-P.; Lane, T.; Pande, V. MDTraj: A Modern Open Library for the Analysis of Molecular Dynamics Trajectories. *Biophysical Journal* **2015**, *109*, 1528–1532, DOI: 10.1016/j.bpj.2015.08.015.

(53) Gowers, R.; Linke, M.; Barnoud, J.; Reddy, T.; Melo, M.; Seyler, S.; Domański, J.; Dotson, D.; Buchoux, S.; Kenney, I.; Beckstein, O. MDAnalysis: A Python Package for the Rapid Analysis of Molecular Dynamics Simulations. Proceedings of the 15th Python in Science Conference. 2016; DOI: 10.25080/majora-629e541a-00e.

(54) Michaud-Agrawal, N.; Denning, E. J.; Woolf, T. B.; Beckstein, O. MDAnalysis: A toolkit for the analysis of molecular dynamics simulations. *Journal of Computational Chemistry* **2011**, *32*, 2319–2327, DOI: 10.1002/jcc.21787.

(55) Vella, J. R.; Marshall, B. D. Mixture Solubility Parameters from Experimental Data

and Perturbed-Chain Statistical Associating Fluid Theory. *Journal of Chemical &; Engineering Data* **2020**, *65*, 5801–5808, DOI: 10.1021/acs.jced.0c00706.

(56) Zhang, H.; Sundaresan, S.; Webb, M. A. Molecular Dynamics Investigation of Nanoscale Hydrophobicity of Polymer Surfaces: What Makes Water Wet? *The Journal of Physical Chemistry B* **2023**, *127*, 5115–5127, DOI: 10.1021/acs.jpcb.3c00616.

(57) Yeh, Y.-l.; Mou, C.-Y. Orientational Relaxation Dynamics of Liquid Water Studied by Molecular Dynamics Simulation. *The Journal of Physical Chemistry B* **1999**, *103*, 3699–3705, DOI: 10.1021/jp984584r.

(58) Fox, T. G. Influence of Diluent and of Copolymer Composition on the Glass Temperature of a Polymer System. *Bulletin of the American Physical Society* **1956**, *1*, 123.

(59) Lyulin, A. V.; Balabaev, N. K.; Michels, M. A. J. Molecular-Weight and Cooling-Rate Dependence of Simulated Tg for Amorphous Polystyrene. *Macromolecules* **2003**, *36*, 8574–8575, DOI: 10.1021/ma034406i.

(60) Soldera, A.; Metatla, N. Glass transition of polymers: Atomistic simulation versus experiments. *Physical Review E* **2006**, *74*, 061803, DOI: 10.1103/physreve.74.061803.

(61) Webb, M. A.; Jung, Y.; Pesko, D. M.; Savoie, B. M.; Yamamoto, U.; Coates, G. W.; Balsara, N. P.; Wang, Z.-G.; Miller, T. F. Systematic Computational and Experimental Investigation of Lithium-Ion Transport Mechanisms in Polyester-Based Polymer Electrolytes. *ACS Central Science* **2015**, *1*, 198–205, DOI: 10.1021/acscentsci.5b00195.

(62) Binder, K.; Block, B. J.; Virnau, P.; Tr oster, A. Beyond the Van Der Waals loop: What can be learned from simulating Lennard-Jones fluids inside the region of phase coexistence. *American Journal of Physics* **2012**, *80*, 1099–1109, DOI: 10.1119/1.4754020.

(63) Humphrey, W.; Dalke, A.; Schulten, K. VMD – Visual Molecular Dynamics. *Journal of Molecular Graphics* **1996**, *14*, 33–38.

TOC Graphic

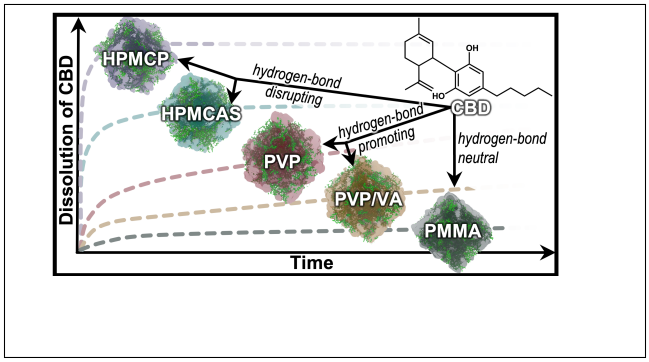
Dissolution of CBD
Time
HPMCP
HPMCAS
PVP
PVP/VA
PMMA
hydrogen-bond disrupting
hydrogen-bond promoting
hydrogen-bond neutral
CBD
OH
HO